SCIENCE CHINA Materials ARTICLES

mater.scichina.com link.springer.com Published online 28 April 2021 | https://doi.org/10.1007/s40843-021-1654-5

Nanochannel-confined growth of crystallographically orientated perovskite nanowire arrays for polarization-sensitive photodetector application

Rui Huang[1], Di-Hua Lin[1], Jia-Yin Liu[1], Chun-Yan Wu[1*], Di Wu[2] and Lin-Bao Luo[1*]

ABSTRACT **Highly ordered perovskite nanowire (PNW) arrays are important building blocks for potential application in integrated optoelectronic devices due to their unique properties. Herein, a recordable digital versatile disk-assisted nanochannel-confined growth (NCG) strategy was developed for large-scale growth of different kinds of PNW arrays with preferentially crystallographic orientation on various substrates. Photodetector constructed from $MAPbI_3$ NW arrays exhibits prominent photoresponse properties with a responsivity of 20.56 A W^{-1} and specific detectivity of 4.73×10^{12} Jones, respectively. What is more, the photodetector can function as a polarization-sensitive photodetector due to the crystallographic orientation of the one-dimensional PNW arrays, with a polarization ratio of 2.2. The proposed NCG strategy provides a cost-efficient and effective method for the fabrication of high-quality PNW arrays with potential applications in future integrated devices and systems.**

Keywords: nanochannel-confined growth, one-dimensional nanostructures, optoelectronic devices, polarization photodetection, template

INTRODUCTION

Metal halide perovskites, including organic-inorganic hybrid perovskites ($MAPbX_3$, $FAPbX_3$, etc., MA=methylammonium, FA = formamidinium, X=Cl, Br, I) and all-inorganic perovskites ($CsPbX_3$, $Cs_3Cu_2I_5$, etc.) have emerged as important candidates for assembly of high-performance optoelectronic devices such as light-emitting devices [1–3], photovoltaics [4–7], and photodetectors [8–11], due to their adjustable bandgap, large optical absorption coefficient, high carrier mobility, and long carrier diffusion length [12–16]. Compared with their film or bulk counterparts, one-dimensional (1D) perovskite nanowires (PNWs) often display attractive physical and optoelectronic merits, such as excellent mechanical stability [17], optical anisotropy in axial and radial directions [18,19], and improved charge carrier transportation [20]. For these reasons, 1D PNWs have recently attracted increasing research interests for their promising applications in ultrasensitive photodetectors [21,22].

Owing to the vulnerability of perovskite materials to humidity and other polar or protic solvents, it is impossible to fabricate PNW arrays *via* conventional photolithography process, followed by harsh developing and etching process in base or organic solutions [23]. Other direct patterning technologies, such as laser direct-write (LDW) method [24], focused ion beam (FIB) etching [25], and inkjet printing technology [26], are indeed capable of fabricating well-defined perovskite arrays. However, the expensive apparatuses as well as the time-consuming process constitute a bottleneck for their practical application. As optional alternatives, some solution-processed strategies have proved to be low-cost and effective patterning approaches [27–29], and to date a number of approaches, such as evaporation-induced self-assembly [18,30], blade-coating method [31] and template confined/induced self-assembly [19,32,33], have been developed for the fabrication of various perovskite nanowire (NW)/microwire (MW) arrays. For example, Deng *et al.* [31] achieved the fabrication of high-quality single-crystalline $MAPbI_3$ MW arrays by a straightforward blade-coating method. The $MAPbI_3$ MW arrays-based photodetector exhibited a high responsivity of 13.57 A W^{-1} as well as excellent flexibility and robust

[1] School of Electronic Science and Applied Physics, Hefei University of Technology, Hefei 230009, China
[2] School of Physics and Microelectronics, Zhengzhou University, Zhengzhou 450052, China
* Corresponding authors (emails: cywu@hfut.edu.cn (Wu CY); luolb@hfut.edu.cn (Luo LB))

bending stability. What is more, well-aligned PNW (e.g., $(BA)_2(MA)_3Pb_4I_{13}$ (BA = butylacrylate) and $CsPbBr_3$) arrays can also be fabricated through an asymmetric-wettability micropillar template. Photodetector made of the $(BA)_2(MA)_3Pb_4I_{13}$ exhibits outstanding photoresponse characteristics, with a responsivity exceeding 1.5×10^4 A W^{-1} and specific detectivity larger than 7×10^{15} Jones [10]. Although the above methods have indeed proved to be effective for the fabrication of PNW arrays, it is undeniable that these methods still suffer from some shortcomings, such as the poor morphology and position control, selective modification with expensive organic molecules or complicated processes including photolithography and etching.

To solve the above-mentioned dilemma, we herein proposed a recordable digital versatile disk (DVD-R)-assisted nanochannel-confined growth (NCG) strategy for large-scale growth of crystallographically orientated nanowire arrays. By taking this strategy, various 1D PNW arrays on different substrates with controllable width (330–660 nm) have been obtained. Further device analysis reveals that photodetector composed of $MAPbI_3$ NW arrays has displayed a responsivity of 20.56 A W^{-1} and specific detectivity of 4.73×10^{12} Jones, which are better than the values of most PNW devices derived from other methods. It is also found that the PNW device is capable of detecting polarized light, with a polarization ratio of 2.2. We believe this work provides a universal approach for the facile and large-scale growth of PNW arrays with preferentially crystallographic orientation, which may have potential applications in future integrated optoelectronic devices.

EXPERIMENTAL SECTION

Fabrication of nanochannel-confined template

The commercial 16× speed 4.7 GB DVD-R used in this work was purchased from Philips Company. The disk was discomposed from the cross-section and the polycarbonate protective layer (layer I) and the metal film reflective layer (layer II) were removed using a blade. Afterwards, the dye recording layer (layer III) was rinsed with ethanol to remove the dye and then blow dried by N_2 flow. The left polycarbonate layer with submicron linear track (layer IV) would be used as the DVD-R master template. A mixture of polydimethylsiloxanes (PDMS) precursor and cross-linker (Sylgard 184, Dow Corning, with a 10:1 weight ratio) was cast onto the master template. After being cured at 60°C for 4 h and peeled off, a PDMS template with parallel nanoscale grooves was obtained, which was cut into 2×2 cm^2 prior to use.

Fabrication of well-aligned PNWPNW arrays

Well-aligned PNW arrays were prepared through the DVD-R-assisted NCG method. The perovskite precursor solutions were prepared by dissolving a 1:1 molar ratio of MAX (or FAX) and PbX_2 (X = Cl, Br, I) in *N*-dimethylformamide (DMF, >99.9%), a 1:1 molar ratio of CsI and PbI_2 (a 3:2 molar ratio of CsI and CuI for $Cs_3Cu_2I_5$) in a mixed solvent of DMF and dimethyl sulfoxide (DMSO, >99.9%) at a volume ratio of 1:1, followed by stirring at 60°C for 12 h. In a typical process for preparing the PNW arrays, the pre-cleaned substrates (e.g. SiO_2/Si, glass, polypropylene (PP) and polyethylene terephthalate (PET)) were firstly treated by oxygen plasma (Harrick PDC-32G-2, 18 W) for 5 min to obtain hydrophilic surfaces. Five microliter of precursor solution was dropped onto the hydrophilic substrate and a thin precursor film will be formed on the surface immediately due to the wetting of the solution on the hydrophilic substrate. A piece of PDMS template was then gently imprinted on the perovskite precursor solution-coated substrate under a moderate pressure (about 10 kPa) provided by the holding equipment shown in Fig. S1. The substrate with PDMS template was kept under ambient conditions for 12 h so that the solvent can be gradually evaporated (the solvent containing DMSO was kept at 70°C for 6 h in a dry oven). The PDMS template was peeled off after the solvent was completely evaporated. Well aligned PNW arrays were formed on the substrate, which were further annealed at 90°C for 15 min for better crystallization.

Structural analysis and device characterization

The compositions and morphologies of the PNW arrays were characterized by X-ray diffraction (XRD, X-Pert PRO MPD, PANalytical) and field emission scanning electron microscopy (FESEM, Hitachi SU8020). The absorption spectrum was recorded on an ultraviolet–visible-near-infrared (UV–NIR) spectrophotometer (Cary 5000). The surface morphology and the topographic profiles of the DVD-R master template, the PDMS template and the obtained PNW arrays were observed by atomic force microscope (AFM, Dimension Icon, Bruker).

For the optoelectronic characterization of the PNW arrays, parallel Au (50 nm) electrodes with a channel width of 18 μm were deposited onto the opposite ends of the NWs by electron beam evaporation through a lab-built shadow mask. Optoelectronic characterization was conducted on a semiconductor characterization system

(Keithley 4200-SCS) equipped with a monochromator (SP 2150, Princeton Co.) under ambient conditions at room temperature. The laser diode with a wavelength of 520 nm (LP520-SF15) was used as light sources and the power intensity was carefully calibrated using a power meter (Thorlabs GmbH., PM 100D) before measurement.

RESULTS AND DISCUSSION

In this strategy, a piece of commercial DVD-R with nanoscale tracks was used as the master template (the internal structure is schematically shown in Fig. S2). The PDMS template with nanochannels was formed by casting a mixture of PDMS precursor and cross-linker onto the DVD-R master template and therefore decently replicating the nanostructures in the DVD-R master template. The detailed fabrication of well-aligned PNW arrays can be learned from Fig. 1a and the Experimental Section. As depicted in the steps II–III of Fig. 1a, when the PDMS template with nanoscale grooves was gently imprinted onto the substrate, the solution on the substrate would be redistributed and confined in the nanochannels formed between the PDMS template and the substrate. The triple-phase contact line was formed at the ends of the nanochannels, where the nucleation of perovskite molecules would occur due to the high surface energy [34]. In the steps IV–V, with the slow evaporation of the solvent, more perovskite molecules in the solution would gradually precipitate out, which would then self-assemble preferentially along the nanochannels, leading to well-aligned PNW arrays [31].

In this study, the decent replication of the nanostructures in the DVD-R master template is vitally important for the successful fabrication of well-defined PNW arrays. To evaluate the effectiveness of the DVD-R-assisted NCG strategy, the surface morphologies of the DVD-R master template and the obtained PDMS template were compared. Fig. 1b and c present the AFM images of the DVD-R master template and the PDMS template, where periodic structures with uniform dimension can be easily observed. As a matter of fact, these periodic gratings are also reflected by the distinct color on both DVD-R master template and the NCG template

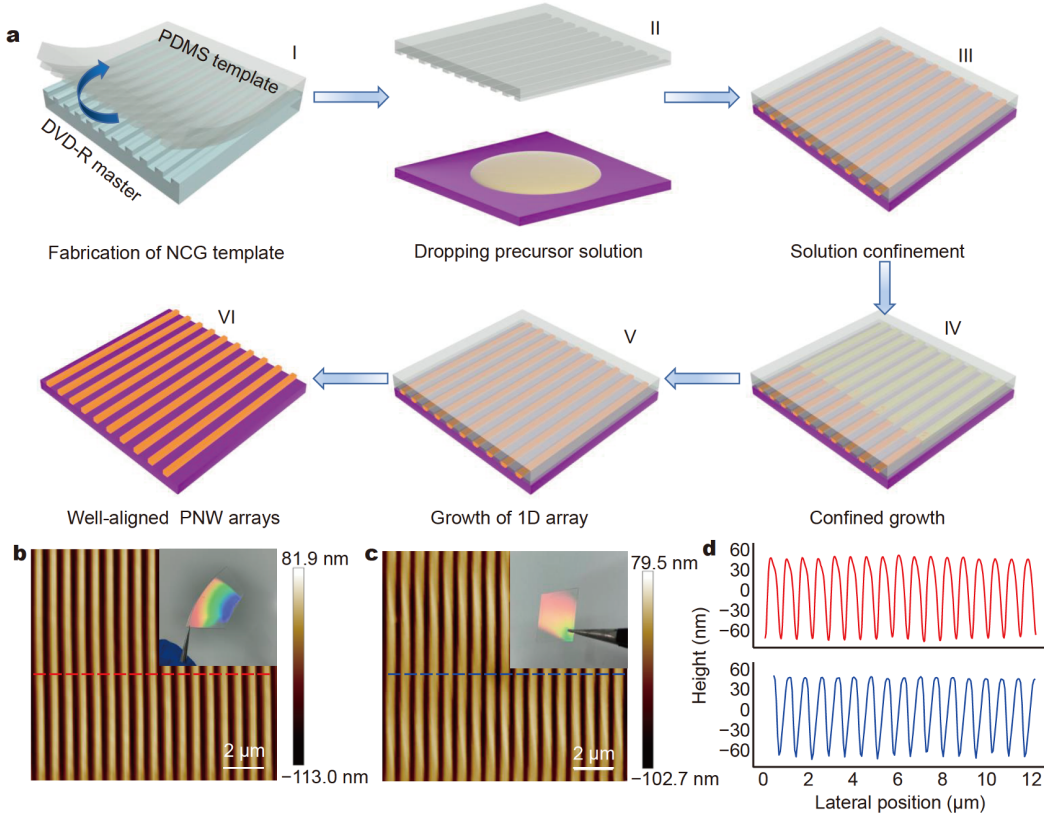

Figure 1 Fabrication of the PNW arrays through a DVD-R-assisted NCG strategy. (a) Schematic illustration of the preparation process for the NCG strategy. AFM images of (b) a representative DVD-R master template and (c) the prepared PDMS template. The insets show the corresponding optical photographs. (d) Topographic profiles across the dotted line in panels (b) and (c).

under sunlight illumination, which should be ascribed to the light-matter interaction (the insets of Fig. 1b, c). According to the corresponding topographic profiles in Fig. 1d, the depth, full width at half maximum (FWHM) and period of the NCG template is about 110, 450 and 760 nm, respectively, which are very close to those of the master template (120, 470 and 760 nm), indicating that the NCG template has replicated the nanostructures of the master template.

The PNW arrays derived from the NCG strategy are characterized by highly ordered arrangement of the nanostructures with nearly identical dimension and morphology. Taking $MAPbI_3$ for example, when using 0.25 mol L^{-1} perovskite solution as precursor, very uniform and well-aligned NW arrays can be observed in the whole field of view (Fig. 2a). The large-scale and homogeneous deposition of ordered PNW arrays on the 1 × 1 cm^2 substrate is confirmed by the optical photograph shown in the inset of Fig. 2a, which exhibits shiny green because of light interference of the well-aligned nanogratings [32]. Further high-magnification SEM images (Fig. 2b, c) reveal that the obtained PNWs have uniform morphology and smooth surface without any apparent defect or distortion, which means that these samples are superior to those previously prepared by the imprinted method [17]. The width and interval of the PNWs is about 430 and 330 nm, respectively, which are smaller than those of the PDMS template due to shrinkage in volume after evaporation. However, the period of the nanograting structures is consistent with that of the nanochannels in the PDMS template (760 nm), verifying the confined growth of PNWs. The XRD pattern of the obtained PNW arrays in Fig. 2d exhibits only two remarkable diffraction peaks located at 14.27° and 28.56°, due to (110) and (220) crystalline planes of $MAPbI_3$, respectively, suggesting the good crystallinity and preferential orientation along the [110] direction [18]. Energy-dispersive X-ray spectroscopy (EDS) element mappings (Fig. 2e) reveal that both Pb and I elements are homogeneously distributed in an individual $MAPbI_3$ NW. The atomic ratio of I/Pb is calculated to be about 2.88 (see Fig. S3), which is very close to the stoichiometric ratio of $MAPbI_3$. Pb or I element can hardly be clearly identified in the region between two adjacent nanowires, confirming the confined growth of PNW array. The AFM image and height profile in Fig. 2f show that all the NWs have a uniform height of about 65 nm, which is lower than the depth of the nanochannels in the PDMS template. We believe this should be ascribed to the evaporation of the solvent confined in the nanochannels of the PDMS template.

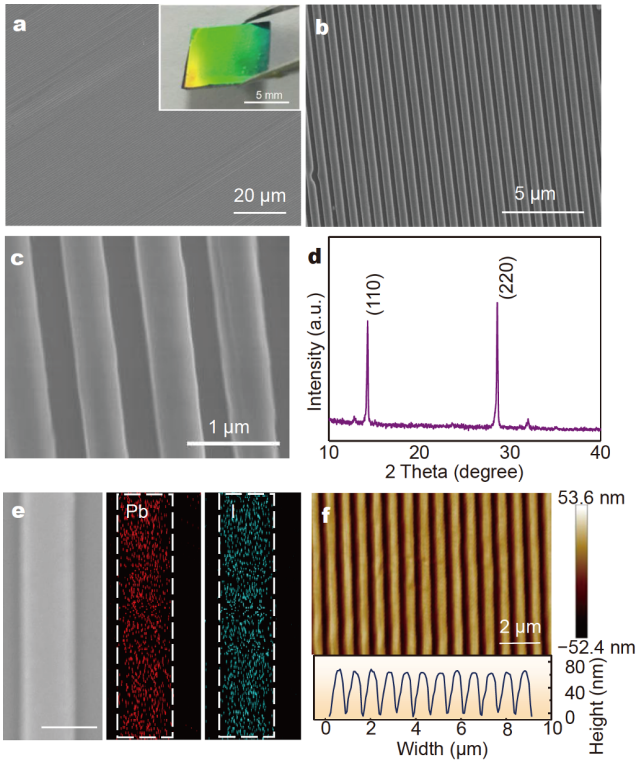

Figure 2 Characterizations of the PNW arrays. (a) Low-, (b) medium-, and (c) high-magnification SEM images of $MAPbI_3$ NW arrays on SiO_2/Si substrate. The inset in panel (a) exhibits the optical photograph of the $MAPbI_3$ NW arrays. (d) XRD pattern of the obtained $MAPbI_3$ NW arrays. (e) A magnified SEM image and corresponding EDS elemental mapping of a single $MAPbI_3$ NW. The scale bar is 500 nm. (f) AFM image (top panel) and the height profile (below panel) of the PNW arrays.

It is noteworthy that the concentration of the precursor solution can directly determine the growth of the PNW arrays in the current DVD-R-assisted NCG strategy [35]. As illustrated in Fig. S4, while the period of PNW arrays remains to be about 760 nm for other concentrations of $MAPbI_3$ precursor solution, the width and the morphology of the NWs vary greatly. For instance, when the concentration decreases from 0.5 to 0.125 mol L^{-1}, the width of the NWs will decrease from 630 to 330 nm (see Fig. S4a–c). This is reasonable as relatively small quantity of perovskite solute would be confined in the nanochannels at low concentrations. When the concentration of perovskite precursor solution further decreases to 0.03 mol L^{-1}, discontinuous PNW arrays will be obtained due to the shortage of solute (see Fig. S4e). These results demonstrate that 1D PNWs with controllable width can be obtained by adjusting the concentration of the precursor solution.

In addition to the above advantages in controlling the diameters of the PNWs, the present NCG strategy also allows the growth of various PNWs (e.g. $MAPbBr_3$, $MAPbCl_3$, $FAPbBr_3$, $FAPbCl_3$ and all-inorganic perovskites such as $CsPbI_3$ and $Cs_3Cu_2I_5$) on SiO_2/Si substrate. The corresponding SEM images (Fig. 3a–f) and XRD patterns (Fig. S5) confirm that the as-obtained samples are all composed of well-aligned PNW arrays with good crystallinity and preferential crystallographic orientation [20,36–38]. Significantly, the PNW arrays can also be grown on other rigid and flexible substrates including glass, PP and PET, as long as these substrates are hydrophilic after surface treatment. Fig. 3g–i show the SEM images of the PNW arrays grown on different substrates, from which well-aligned NW arrays with smooth surface and uniform morphology are observed. Like the PNW arrays on SiO_2/Si substrate, similar shiny color due to strong light interference can be observed for all the obtained PNW arrays, indicative of formation of large-area well-aligned nanograting structures. The excellent adaptability of this method for substrates stems from the good flexibility of PDMS material, which allows it to form intimate contact with the underlying substrate [39,40]. In addition, within the nanochannel, the slow volatilization of solvent can facilitate the gradual precipitation and deposition of the perovskite molecules on the substrate, which is vitally important for the growth of high-quality PNW arrays.

Various studies have shown that high-quality, crystallographically orientated nanostructures may provide a direct axial transportation path for the charged carriers, which may facilitate their applications in optoelectronic devices [20,41,42]. In light of this, we then assembled photodetectors based on the well-aligned $MAPbI_3$ PNW arrays, in an effort to explore their potential applications for optoelectronic devices. Fig. 4a illustrates the device geometry of a typical photodetector based on $MAPbI_3$ NW arrays and the optical photograph of a typical device with a channel width of 18 μm (Fig. S6). It is seen that once the device was illuminated by 520 nm incident light, it exhibited remarkable photoresponse, with the photocurrent increasing monotonously as the incident light power density increased from 3.48 μW cm^{-2} to 1.45 mW cm^{-2}. This evolution is reasonable since more photon-induced carriers would be generated at high incident light power densities. The dependence of the net photocurrent ($I_{ph} = I_{light} - I_{dark}$, where I_{light} is the photocurrent and I_{dark} is the dark current) on power density (P) can be described by using a general power law ($I_{ph} \propto P^{\theta}$), where the exponent θ is the empirical value reflecting the

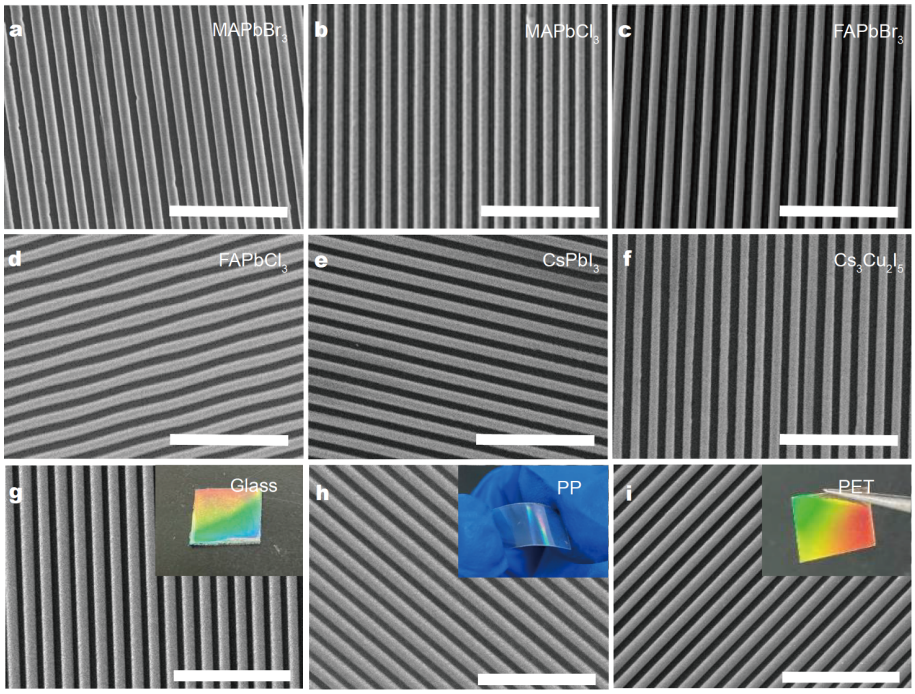

Figure 3 The universality of the NCG strategy. Different kinds of PNW arrays including (a) $MAPbBr_3$, (b) $MAPbCl_3$, (c) $FAPbBr_3$, (d) $FAPbCl_3$, (e) $CsPbI_3$ and (f) $Cs_3Cu_2I_5$ deposited on SiO_2/Si substrate and $MAPbI_3$ NW arrays deposited on (g) glass, (h) PP and (i) PET. The insets show the corresponding optical photographs of the PNW arrays in panels (g–i). The scale bars are 5 μm.

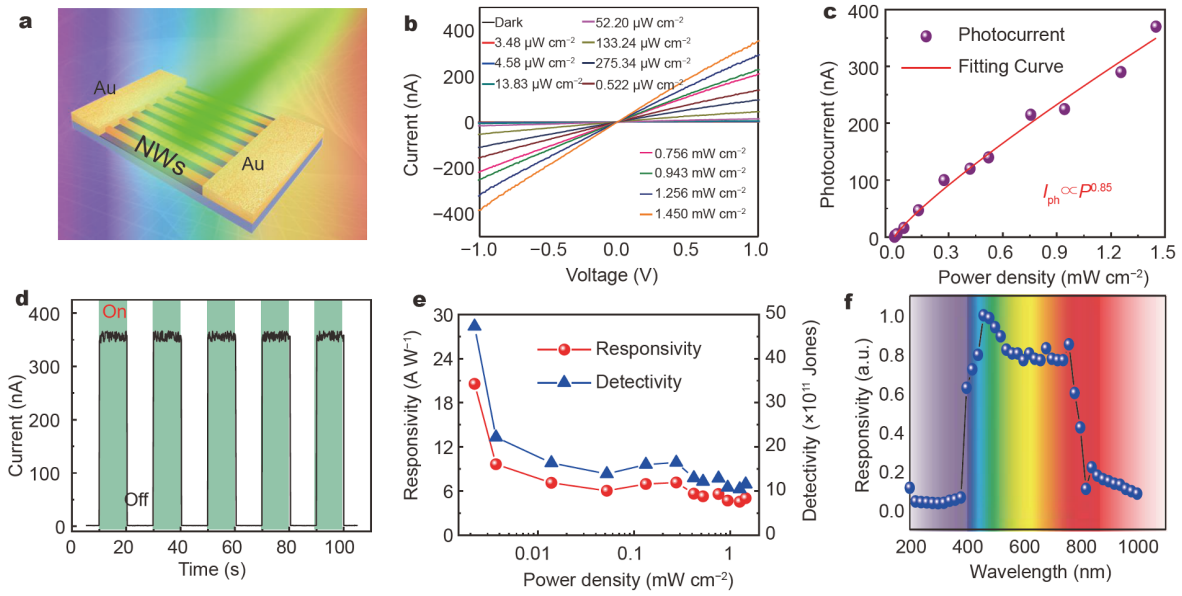

Figure 4 Optoelectronic properties of the PNW arrays. (a) Schematic illustration of the aligned $MAPbI_3$ NW arrays-based photodetector. (b) Current-voltage (*I-V*) curves of a typical photodetector in dark and upon 520 nm illumination with varied incident light power densities from 3.48 μW cm^{-2} to 1.45 mW cm^{-2}. (c) Photocurrent as a function of the power density. (d) Time-dependent photoresponse of the device under 520 nm light illuminations (1.45 mW cm^{-2}) at the bias voltage of 1 V. (e) Dependence of responsivity and specific detectivity on the power density. (f) Spectral response of the device in the wavelength range of 200–1000 nm.

recombination of the photo-generated carriers and would be determined by the linear relationship of incident light power density and photocurrent (Fig. 4c) [43]. Fitting the experimental result leads to a non-integral θ of 0.85, signifying the complicated process of electron-hole generation, trapping and recombination loss during the photodetection process [43,44]. Specifically, the device displays steady and repeatable switching characteristics between the high- and low-resistance states (Fig. 4d). The dark current is around 0.3 nA while the current rises sharply to 350 nA upon light illumination, yielding a high I_{light}/I_{dark} ratio of about 1.2×10^3. Compared with the polycrystalline thin film-based photodetector, the I_{dark} in this study is higher. This is understandable since the as-fabricated PNWs are characterized by few grain boundaries which fail to suppress the dark current [11,17]. In addition, photodetectors assembled from some other PNW arrays, including $MAPbBr_3$, $MAPbCl_3$, $FAPbBr_3$, $FAPbCl_3$, $CsPbI_3$ and $Cs_3Cu_2I_5$, have also exhibited well-defined photoresponses (Fig. S7).

The responsivity (R) of the as-fabricated photodetector was evaluated and can be given by $R = I_{ph}/PS$, where S is the effective device area [45]. R is calculated to be 20.56 A W^{-1} (net photocurrent $I_{ph} \approx 2.3$ nA, $S \approx 5 \times 10^{-5}$ cm^2) under 520 nm light illumination (incident light power density: 2.2 μW cm^{-2}). According to the calculated value of R, the specific detectivity (D^*) for the PNW arrays-based device is calculated to be 4.73×10^{12} Jones by using the equation $D^* = RS^{1/2}/(2eI_{dark})^{1/2}$, where e is the electron charge (1.6×10^{-19} C) [46]. Table 1 lists R and D^* of the present device and other $MAPbI_3$-based photodetectors. It is seen that while the specific detectivity is comparable to other NWs-based devices, the responsivity is higher than most of devices listed in the table [18,30,31], except for the one composed of NWs derived from fluid-guided antisolvent vapor-assisted crystallization method [22]. Such relatively good device performance is related to the reduced grain boundary and defects in the obtained PNW arrays. Both R and D^* are found to decrease as power density increases (Fig. 4e), indicative of intensified recombination loss at relatively high intensity [19]. In addition, the external quantum efficiency (EQE), defined as the ratio between the number of photoexcited electron-hole pairs and the number of incident photons, has been calculated according to the equation EQE = $(hcR/e\lambda) \times 100\%$, where h is the Planck constant, c and λ represent the speed of light and the incident light wavelength, respectively [45]. The value of EQE reaches a maximum 4.89×10^3% (see Fig. S8), which means that internal gain plays a significant role in such a photoconductive device. Although it tends to decrease with increasing power density, it exceeds 1000% under all

Table 1 Comparison of the performance between our photodetector and other $MAPbI_3$-based devices

Device structure	Measurement conditions	R (A W^{-1})	D^* (Jones)	Ref.
$MAPbI_3$ MW	V = −5 V; λ = 420 nm, 1 μW cm^{-2}	13.57	5.25 × 10^{12}	[31]
$MAPbI_3$ NW	V = 1 V; λ = 650 nm, 4 μW cm^{-2}	0.85	2.5 × 10^{12}	[30]
$MAPbI_3$ NW	V = 1 V; λ = 530 nm, 2.5 nW cm^{-2}	4.95	2 × 10^{13}	[18]
$MAPbI_3$ NW	V = 5 V; λ = 550 nm, 0.1 μW cm^{-2}	1.25 × 10^4	1.73 × 10^{11}	[22]
$MAPbI_3$ NW	V = 1 V; λ = 520 nm, 2.2 μW cm^{-2}	20.56	4.73 × 10^{12}	Our work

tested conditions. To further unveil the dependence of responsivity on the wavelength of the incident light, normalized spectral response of the photodetector was recorded in the wavelength range of 200–1000 nm at a fixed power density (50 μW cm^{-2}). As we can see from Fig. 4f, the device exhibits a broadband photoresponse in the visible light region, but relatively weak photoresponse for wavelengths longer than 800 nm, which is consistent with previously reported results [18,22].

A number of 1D semiconductor nanostructures have demonstrated promising application for polarization-sensitive photodetectors, due to their anisotropic optical absorption arising from the high aspect ratio and oriented crystallization [47,48]. To further explore the possibility of current well-aligned $MAPbI_3$ NW arrays for polarization-dependent detection application, the optoelectronic property was then studied by shining a polarized light that is generated using a polarizer and can be continually rotated to change the polarization angle of the incident light. Apparently, the photocurrent exhibits a strong dependence on the polarization angle (Fig. 5b, c). The maximum photocurrent emerges with the polarization angle of 0° when the polarization direction is parallel to the axial direction of the PNW. With the increase of the polarization angle, the photocurrent gradually decreases until it achieves a minimum value at the polarization angle of 90°. Further increase of polarization angle leads to a continuous increase in photocurrent until the po-

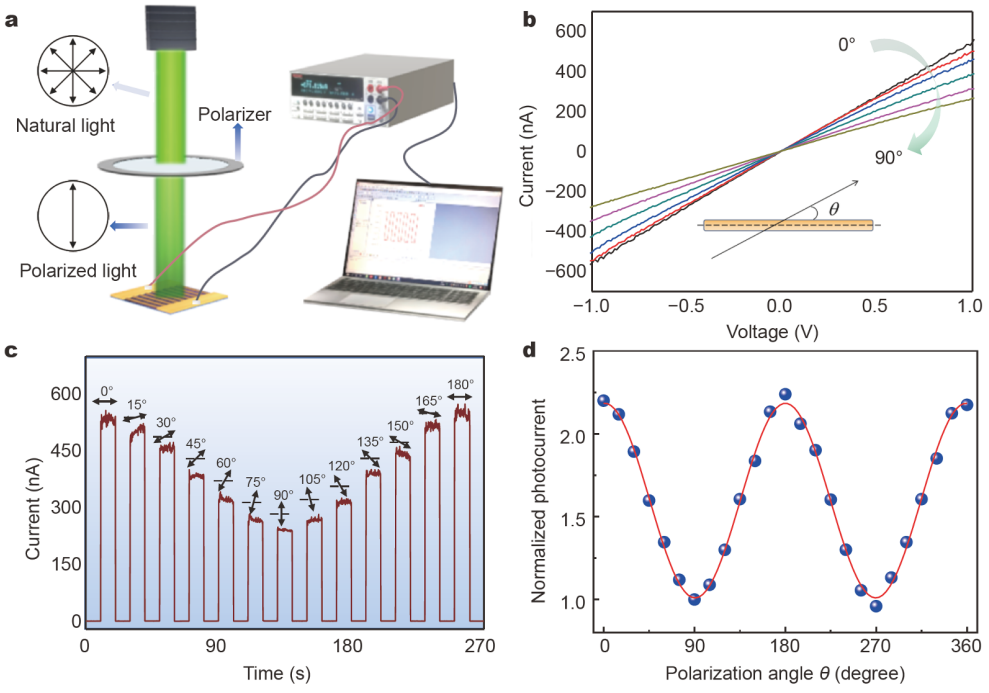

Figure 5 Application in the photodetection of polarized light. (a) Schematic diagram of measurement configuration for the polarization photodetection. (b) *I-V* curves under incident light with different polarization angles. The polarization angle (θ) is defined as the angle between the incident light polarized direction and the axial direction of the PNW arrays. (c) Time-dependent photoresponses under incident light with different polarization angles. (d) Normalized photocurrent as a function of the polarization angle θ. The unity corresponds to the photocurrent with the polarization angle of 90°.

larization angle reaches 180°. Normalized polarization-dependent photocurrent is depicted in Fig. 5d, which exhibits a decent cosine wave and illustrates a polarization ratio of 2.2. This value is higher than that of oleic acid-passivated single-crystalline $MAPbI_3$ NWs (1.3) [18] and comparable to those of inorganic single-crystalline $CsPbBr_3$ NWs (2.6) [19] and β-$CsPbI_3$ NWs (2.68) [44].

CONCLUSIONS

In summary, we have demonstrated a DVD-R-assisted NCG strategy for the facile and versatile fabrication of large-scale well-aligned PNW arrays with preferential crystallographic orientation by directly growing the perovskite precursor within the nanochannel. Without the assistance of a traditional photolithography process, this strategy shows excellent compatibility which allows the controlled growth of various PNWs on both rigid and flexible substrates. Further analysis reveals that the photodetector based on $MAPbI_3$ NW arrays exhibits obvious photoresponse properties with a responsivity of 20.56 A W^{-1} and specific detectivity of 4.73×10^{12} Jones upon 520 nm illumination, respectively, which are much better than previously reported values. This relatively good optoelectronic performance should be attributed to the high-quality crystallinity and the highly oriented 1D nanostructure which provide an effective transport pathway for the photogenerated carriers. Meanwhile, the PNW array photodetector is also very sensitive to polarization light, with a polarization ratio of 2.2. The proposed NCG strategy proves to be a cost-efficient and effective method for fabrication of high-quality PNW arrays with potential applications in integrated optoelectronic devices and systems.

Received 19 January 2021; accepted 22 February 2021; published online 28 April 2021

1 Ling Y, Yuan Z, Tian Y, *et al.* Bright light-emitting diodes based on organometal halide perovskite nanoplatelets. Adv Mater, 2016, 28: 305–311
2 Tan ZK, Moghaddam RS, Lai ML, *et al.* Bright light-emitting diodes based on organometal halide perovskite. Nat Nanotech, 2014, 9: 687–692
3 Lin P, Chen H, Wei Z, *et al.* Continuous-flow synthesis of doped all-inorganic perovskite nanocrystals enabled by a microfluidic reactor for light-emitting diode application. Sci China Mater, 2020, 63: 1526–1536
4 Zhou H, Chen Q, Li G, *et al.* Interface engineering of highly efficient perovskite solar cells. Science, 2014, 345: 542–546
5 Grätzel M. The light and shade of perovskite solar cells. Nat Mater, 2014, 13: 838–842
6 Green MA, Ho-Baillie A, Snaith HJ. The emergence of perovskite solar cells. Nat Photon, 2014, 8: 506–514
7 Liu Z, Ono LK, Qi Y. Additives in metal halide perovskite films and their applications in solar cells. J Energy Chem, 2020, 46: 215–228
8 Hu X, Zhang X, Liang L, *et al.* High-performance flexible broadband photodetector based on organolead halide perovskite. Adv Funct Mater, 2014, 24: 7373–7380
9 Xue M, Zhou H, Xu Y, *et al.* High-performance ultraviolet-visible tunable perovskite photodetector based on solar cell structure. Sci China Mater, 2017, 60: 407–414
10 Feng J, Gong C, Gao H, *et al.* Single-crystalline layered metal-halide perovskite nanowires for ultrasensitive photodetectors. Nat Electron, 2018, 1: 404–410
11 Lian Z, Yan Q, Lv Q, *et al.* High-performance planar-type photodetector on (100) facet of $MAPbI_3$ single crystal. Sci Rep, 2015, 5: 16563
12 Lee MM, Teuscher J, Miyasaka T, *et al.* Efficient hybrid solar cells based on meso-superstructured organometal halide perovskites. Science, 2012, 338: 643–647
13 Stranks SD, Eperon GE, Grancini G, *et al.* Electron-hole diffusion lengths exceeding 1 micrometer in an organometal trihalide perovskite absorber. Science, 2013, 342: 341–344
14 Xing G, Mathews N, Sun S, *et al.* Long-range balanced electron- and hole-transport lengths in organic-inorganic $CH_3NH_3PbI_3$. Science, 2013, 342: 344–347
15 Stoumpos CC, Malliakas CD, Kanatzidis MG. Semiconducting tin and lead iodide perovskites with organic cations: phase transitions, high mobilities, and near-infrared photoluminescent properties. Inorg Chem, 2013, 52: 9019–9038
16 Hodes G. Perovskite-based solar cells. Science, 2013, 342: 317–318
17 Cao F, Tian W, Wang M, *et al.* Semitransparent, flexible, and self-powered photodetectors based on ferroelectricity-assisted perovskite nanowire arrays. Adv Funct Mater, 2019, 29: 1901280
18 Gao L, Zeng K, Guo J, *et al.* Passivated single-crystalline $CH_3NH_3PbI_3$ nanowire photodetector with high detectivity and polarization sensitivity. Nano Lett, 2016, 16: 7446–7454
19 Feng J, Yan X, Liu Y, *et al.* Crystallographically aligned perovskite structures for high-performance polarization-sensitive photodetectors. Adv Mater, 2017, 29: 1605993
20 Chen G, Feng J, Gao H, *et al.* Stable α-$CsPbI_3$ perovskite nanowire arrays with preferential crystallographic orientation for highly sensitive photodetectors. Adv Funct Mater, 2019, 29: 1808741
21 Gu L, Poddar S, Lin Y, *et al.* A biomimetic eye with a hemispherical perovskite nanowire array retina. Nature, 2020, 581: 278–282
22 Deng W, Huang L, Xu X, *et al.* Ultrahigh-responsivity photodetectors from perovskite nanowire arrays for sequentially tunable spectral measurement. Nano Lett, 2017, 17: 2482–2489
23 Wang S, Jiang Y, Juarez-Perez EJ, *et al.* Accelerated degradation of methylammonium lead iodide perovskites induced by exposure to iodine vapour. Nat Energy, 2017, 2: 16195
24 Chou SS, Swartzentruber BS, Janish MT, *et al.* Laser direct write synthesis of lead halide perovskites. J Phys Chem Lett, 2016, 7: 3736–3741
25 Alias MS, Dursun I, Shi D, *et al.* Focused-ion beam patterning of organolead trihalide perovskite for subwavelength grating nanophotonic applications. J Vacuum Sci Tech B, 2015, 33: 051207
26 Gu Z, Wang K, Li H, *et al.* Direct-writing multifunctional perovskite single crystal arrays by inkjet printing. Small, 2017, 13: 1603217
27 Lee W, Lee J, Yun H, *et al.* High-resolution spin-on-patterning of

perovskite thin films for a multiplexed image sensor array. Adv Mater, 2017, 29: 1702902
28 Lee L, Baek J, Park KS, *et al.* Wafer-scale single-crystal perovskite patterned thin films based on geometrically-confined lateral crystal growth. Nat Commun, 2017, 8: 15882
29 Spina M, Bonvin E, Sienkiewicz A, *et al.* Controlled growth of $CH_3NH_3PbI_3$ nanowires in arrays of open nanofluidic channels. Sci Rep, 2016, 6: 19834
30 Deng H, Dong D, Qiao K, *et al.* Growth, patterning and alignment of organolead iodide perovskite nanowires for optoelectronic devices. Nanoscale, 2015, 7: 4163–4170
31 Deng W, Zhang X, Huang L, *et al.* Aligned single-crystalline perovskite microwire arrays for high-Performance flexible image sensors with long-term stability. Adv Mater, 2016, 28: 2201–2208
32 Jeong B, Hwang I, Cho SH, *et al.* Solvent-Assisted gel printing for micropatterning thin organic–inorganic hybrid perovskite films. ACS Nano, 2016, 10: 9026–9035
33 Liu P, He X, Ren J, *et al.* Organic–inorganic hybrid perovskite nanowire laser arrays. ACS Nano, 2017, 11: 5766–5773
34 Kunkelmann C, Ibrahem K, Schweizer N, *et al.* The effect of three-phase contact line speed on local evaporative heat transfer: Experimental and numerical investigations. Int J Heat Mass Transfer, 2012, 55: 1896–1904
35 Li SX, Xu YS, Li CL, *et al.* Perovskite single-crystal microwire-array photodetectors with performance stability beyond 1 year. Adv Mater, 2020, 32: 2001998
36 Yu W, Li F, Yu L, *et al.* Single crystal hybrid perovskite field-effect transistors. Nat Commun, 2018, 9: 5354
37 Levchuk I, Osvet A, Tang X, *et al.* Brightly luminescent and color-tunable formamidinium lead halide perovskite $FAPbX_3$ (X = Cl, Br, I) colloidal nanocrystals. Nano Lett, 2017, 17: 2765–2770
38 Chen H, Pina JM, Yuan F, *et al.* Multiple self-trapped emissions in the lead-free halide $Cs_3Cu_2I_5$. J Phys Chem Lett, 2020, 11: 4326–4330
39 Kim A, Jang KS, Kim J, *et al.* Solvent-free directed patterning of a highly ordered liquid crystalline organic semiconductor via template-assisted self-assembly for organic transistors. Adv Mater, 2013, 25: 6219–6225
40 Hassanin H, Mohammadkhani A, Jiang K. Fabrication of hybrid nanostructured arrays using a PDMS/PDMS replication process. Lab Chip, 2012, 12: 4160–4167
41 Duan X, Huang Y, Cui Y, *et al.* Indium phosphide nanowires as building blocks for nanoscale electronic and optoelectronic devices. Nature, 2001, 409: 66–69
42 Agarwal R, Lieber CM. Semiconductor nanowires: optics and optoelectronics. Appl Phys A, 2006, 85: 209–215
43 Kind H, Yan H, Messer B, *et al.* Nanowire ultraviolet photodetectors and optical switches. Adv Mater, 2002, 14: 158–160
44 Zhou Y, Luo J, Zhao Y, *et al.* Flexible linearly polarized photodetectors based on all-inorganic perovskite $CsPbI_3$ nanowires. Adv Opt Mater, 2018, 6: 1800679
45 Choi MS, Qu D, Lee D, *et al.* Lateral MoS_2 p–n junction formed by chemical doping for use in high-performance optoelectronics. ACS Nano, 2014, 8: 9332–9340
46 Choi W, Cho MY, Konar A, *et al.* High-detectivity multilayer MoS_2 phototransistors with spectral response from ultraviolet to infrared. Adv Mater, 2012, 24: 5832–5836
47 Wang J, Gudiksen MS, Duan X, *et al.* Highly polarized photoluminescence and photodetection from single indium phosphide nanowires. Science, 2001, 293: 1455–1457
48 Singh A, Li X, Protasenko V, *et al.* Polarization-sensitive nanowire photodetectors based on solution-synthesized CdSe quantum-wire solids. Nano Lett, 2007, 7: 2999–3006

Acknowledgements This work was supported by the National Natural Science Foundation of China (NSFC, 62074048), the Fundamental Research Funds for the Central Universities (PA2020GDKC0014, JZ2020HGTB0051, and JZ2018HGXC0001), and the Open Foundation of Anhui Provincial Key Laboratory of Advanced Functional Materials and Devices (4500-411104/011).

Author contributions Luo LB supervised the project; Huang R conceived the idea and carried out the sample fabrication and device measurements; Liu JY prepared the PDMS template and precursor solutions; Huang R and Lin DH conducted the optical, XRD, AFM and SEM characterizations; Huang R, Wu CY and Luo LB co-wrote the paper. Wu D provided guidance in the experiments and characterizations. All the authors discussed the results, commented on and revised the manuscript.

Conflict of interest The authors declare that they have no conflict of interest.

Supplementary information Supplementary information and supporting data are available in the online version of the paper.

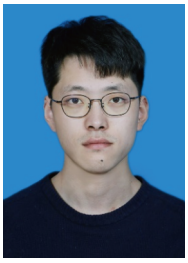

Rui Huang received his Bachelor degree from Hefei University of Technology, China. He is currently a graduate student at the School of Electronic Sciences and Applied Physics, Hefei University of Technology, China. His main research interest focuses on optoelectronic devices based on perovskite materials.

Chun-Yan Wu received her PhD degree in inorganic chemistry from the University of Science and Technology of China in 2006. She is currently a professor at the School of Electronic Science and Applied Physics, Hefei University of Technology, Hefei, China. Her research interests involve 2D layered semiconductors, photoelectronic devices and applications of photodetector arrays for integrated optoelectronic systems.

Lin-Bao Luo received his PhD degree from the Department of Physics and Materials Sciences, City University of Hong Kong under the guidance of Prof. Shuit-Tong Lee in 2009. After spending one and half years in the same group as a research associate, he joined the School of Electronic Sciences and Applied Physics, Hefei University of Technology, where he is now a full professor of applied physics. His research interest mainly focuses on high-performance optoelectronic and electronic device applications including photodetectors (UV light, NIR), photovoltaic devices, and nonvolatile memory devices etc.

纳米通道限域生长制备取向生长的钙钛矿纳米线阵列及其在偏振光探测方面的应用

黄瑞[1], 林笛嫣[1], 刘佳音[1], 吴春艳[1*], 吴翟[2], 罗林保[1*]

摘要 有序排列、取向生长的钙钛矿纳米线阵列的合成通常需要复杂的工艺条件和精密的仪器设备, 这不利于其广泛应用. 本文提出了一种纳米通道限域生长的方法来制备钙钛矿纳米线阵列. 利用场发射扫描电子显微镜、原子力显微镜和X射线衍射等分析手段, 表征了纳米线阵列的形貌和晶体结构, 证明了该方法可用于在各种衬底上制备大面积的具有取向生长特点的不同种类的钙钛矿纳米线阵列. 基于$MAPbI_3$纳米线阵列所制备的光电探测器光响应优异, 响应度和比探测率分别为20.56 A W^{-1}和4.73 × 10^{12} Jones. 此外, 由于所制备的一维钙钛矿纳米线结构的各向异性, 该光电探测器还实现了对于偏振光的探测, 其偏振比为2.2.